

Coarse Grained Simulation and Dynamic Bridging for Turbulent Mixing Predictions

Fernando F. Grinstein
fgrinstein@lanl.gov

Los Alamos National Laboratory, Los Alamos, NM 87545, USA.

Abstract: We revisit coarse-grained simulation strategies for turbulent material mixing driven by shocked / accelerated material interfaces, based on LANL's Radiation Adaptive Grid Eulerian (xRAGE) – Implicit Large-Eddy Simulation (ILES), and dynamic bridging xRAGE-ILES and Besnard-Harlow-Rauenzahn (BHR) – Reynolds-Averaged Navier-Stokes (RANS), using Low-Mach-Corrected (LMC) xRAGE hydrodynamics. Tests of the new simulation paradigms demonstrate improved scale-resolving, enabling higher simulated mixing and turbulence levels on coarser grids. Impact assessments are carried out based on simulations of shock-tube experiments.

Keywords: shock driven turbulence, large eddy simulation.

1 Introduction

In shock-driven turbulence applications such as inertial-confinement-fusion capsule-implosion experiments, we are interested in predicting the mixing consequences of material interpenetration and hydro-dynamical instabilities arising from perturbations at shocked/accelerated material interfaces. The 3D variable-density hydrodynamics depends on initial conditions (IC) and involves transition to turbulence, non-equilibrium turbulence development, and late-time relaminarization. Such flow physics can be captured with a coarse grained simulation paradigm [1], presuming the spectral cascade transfer of energy (*the rate limiting step*) is determined by the initial and boundary condition constrained large-scale dynamics, and using mixing transition criteria and effective turbulence Reynolds numbers (Re) for macroscopic convergence metrics [2]. Because shocks and turbulence are involved, resolving all relevant physical scales in shock-driven turbulence simulations becomes prohibitively expensive. ILES addresses the seemingly insurmountable issues posed by underresolution [4] by combining shock and turbulence emulation capabilities based on a single numerical model [1].

Strategies bridging large-eddy simulation (LES) and RANS are the aerospace and automobile industry standard for full scale simulations [5]. Blended hybrids such as the Flow Simulation Methodology [6, 7] scale the closure terms on the RANS equations by a contribution function $0 < f(\Delta/L) < 1$, where Δ is the local grid size, and L is a reference bridging length. Balance between modeled and computed dissipation is based on the RANS stress model R_{ij}^m locally morphing into SGS Favre-averaged LES stress SGS model \tilde{R}_{ij}^s ,

$$\tilde{R}_{ij}^s \equiv f(\Delta/L) R_{ij}^m, \quad (1)$$

where the contribution function $f(\Delta/L)$ vanishes in the high fidelity limit ($\Delta \rightarrow 0$) and approaches unity at the low resolution limit (pure RANS). Formal relations such as (1) – involving ensemble-averaged RANS and spatially-filtered LES quantities, are interpreted in a generalized-function (integral) sense. Hybrids exploit the structural similarity of equations for RANS and LES, and use relationships between filtering and averaging operations [8].

FSM was originally intended to locally bridge direct numerical simulation (DNS) and RANS as a function of grid resolution. More generally, FSM can be used to locally blend a high-fidelity simulation strategy such

as ILES with RANS to generate a sophisticated LES strategy in-between. The issue of interest is the computation of the dissipation which has to be supplemented by the model for underresolved flow conditions. For sufficiently fine resolution the dissipation range is resolved and the RANS contribution should switch itself off – i.e., $f(\Delta/L) \rightarrow 0$ as $\Delta \rightarrow 0$. In the FSM approach first proposed in [6] – and subsequently pursued in various forms by others, empirical *ad hoc* forms for the contribution function f were prescribed.

Dynamically solving for f based on decomposing the full stress into modeled and resolved components and using a differential filter as secondary filtering operation to define the resolved part was first proposed in [9], and recently extended [12, 13] by additionally requiring the resolved stress to approach the full stress with grid resolution refinement to ensure realizability of the bridging-based LES. In our dynamic FSM paradigm for turbulent material mixing applications, the full stress is decomposed in terms of modeled \tilde{R}_{ij}^s and resolved T_{ij} parts,

$$R_{ij}^{full} = \tilde{R}_{ij}^s + T_{ij} . \quad (2)$$

We use ILES as high-resolution limit strategy in the formalism, so there is no explicit LES SGS model, and the hybrid \tilde{R}_{ij}^s is directly related to the RANS stress R_{ij}^m in terms of f through (1).

For consistency and realizability of the generated LES in approaching the high resolution / fidelity limit, we require that $T_{ij} \rightarrow R_{ij}^{full}$ as $\Delta/L \rightarrow 0$. We enforce this additional modeling constraint, in terms of $\gamma = (\Delta/L)^l$, for $l \geq 1$, by assuming that R_{ij}^{full} can be approximated by a resolution-dependent weighted-average of the RANS and resolved stresses,

$$R_{ij}^{full} \sim \gamma R_{ij}^m + (1 - \gamma)T_{ij} . \quad (3)$$

We substitute equation (1) into (2), use (3), and after contracting with a generic tensor quantity q_{ij} – e.g., $q_{ij} = T_{ij}$, we solve for f – see full derivations in [12, 13],

$$f(\Delta/L) = \gamma \{ 1 - [q_{ij}T_{ij}] / [q_{ij}R_{ij}^m] \} . \quad (4)$$

For consistency we also require $f \equiv 1$ for $\gamma \geq 1$.

By design, the contribution function enforces realizability of the bridging-based LES through (1) in the high fidelity limit $\Delta \rightarrow 0$ when LES \rightarrow DNS. The choice of l controls how the numerics-based ILES SGS model is supplemented by the explicit SGS model generated by the bridging strategy for intermediate resolutions. For xRAGE numerics – 1st-order near shocks and 2nd-order in smooth flow regions, $l \geq 2$ is a suitable choice.

Present ILES is based on the newly available directionally-unsplit LMC xRAGE numerical hydrodynamics [11, 12, 13, 14]. The default 2nd-order split xRAGE hydrodynamics [15] was used in our earlier *sequential* ILES/RANS simulations of the CEA shock-tube laboratory experiments [16] running pure ILES at early times to generate RANS initialization at a selected prescribed start time. In contrast, the present dynamic bridging LES/RANS paradigm acts at all times as the reference ILES.

The Dynamic BHR formalism uses the Besnard-Harlow-Rauenzahn (BHR) multi-equation RANS framework [25] in the BHR3.0 version [26, 24]. Similar BHR extensions with the more recent BHR3.1 [27] version are expected to be straightforward. Detailed discussion of BHR initialization issues can be found in [12, 13].

In the original FSM modeling bridging DNS and RANS [6, 7], the bridging lengthscale L was an estimated Kolmogorov length scale. Choosing $L \sim$ Kolmogorov scale amounts to choosing L as the smallest hydrodynamic length-scale in the turbulent flow, or, a small fraction of the Taylor microscale characterizing the smallest vortices of the turbulence. Likewise, for bridging ILES and RANS, a computed Taylor microscale of the velocity fluctuations (λ_c) characterizing the CGS cutoff and simulated turbulence can be usefully considered (see Fig.6). Such computed Taylor microscale λ_c can be directly evaluated in terms of suitable volumetric-averaged functions of the raw velocity data $\{u_i\}$, [17] by

$$\lambda_c = \left[\sum_{i=1}^{i=3} \sqrt{\langle u_i^2 \rangle / \langle u_{i,i}^2 \rangle} \right] / 3; \quad (5)$$

As λ_c is typically found to be $\gtrsim 10$ cells for xRAGE ILES [18], choices of $L \sim$ few cells in what follows, amount to choosing L as small fraction of λ_c .

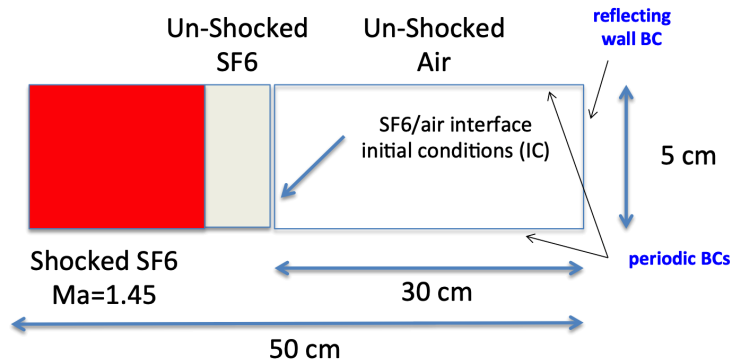


Figure 1: Schematic of the CEA planar shock tube configuration.

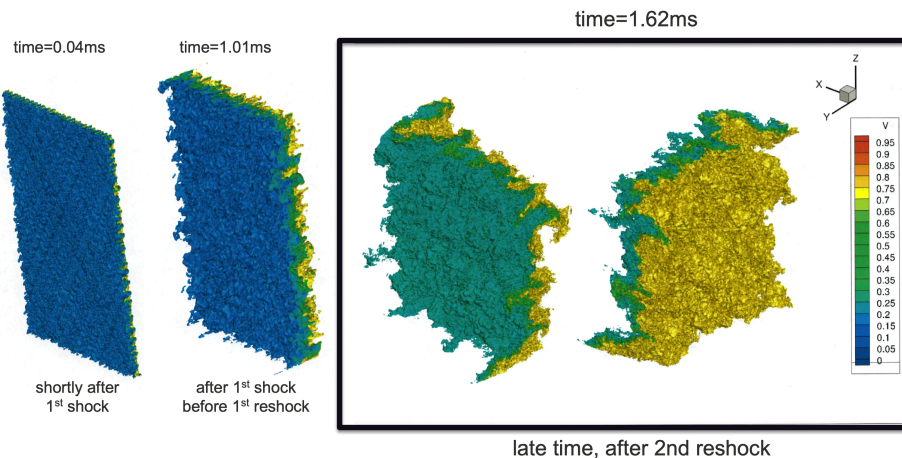


Figure 2: SF_6 mass-fraction isosurface visualizations of 0.05mm resolution ILES predictions.

2 CEA Planar Shock Tube

We revisit the CEA shock-tube laboratory experiments [19], involving high (SF_6) and low (air) density gases, Atwood number, $At = 0.67$, presumed geometries of the membranes and the wire mesh initially separating the gases, and reshock off an end-wall. A shocked SF_6 region is created upstream in terms of a higher-density higher-pressure SF_6 region for a Mach 1.45 shock (strength 0.54). The planar primary shock propagates through unshocked SF_6 , and then through the SF_6 /Air contact discontinuity. The shock effects at the end of the simulation box where purely reflecting boundary conditions are enforced – to enable reshock simulation (Fig. 1).

In the recent *sequential* xRAGE-ILES/BHR-RANS hybrid simulation studies [16], xRAGE-ILES generated data was used to provide physics-based IC to BHR-RANS just before 1st reshock, and was also used as reference for its assessment. By prescribing ILES generated 3D and allowing for 3D convection with just enough resolution in [16], the computed dissipation in 3D RANS (vs. 2D RANS) was found to effectively supplement the modeled dissipation following 1st reshock. However, the 3D RANS cannot resolve well the subsequent consequences of a new transitional flow event at 2nd reshock [16]. This limitation is typical of a standalone RANS and motivates our pursuit of suitable *blended* LES/RANS capable of dynamically adapting the simulation model to local flow conditions for applications driven by multiple shocks.

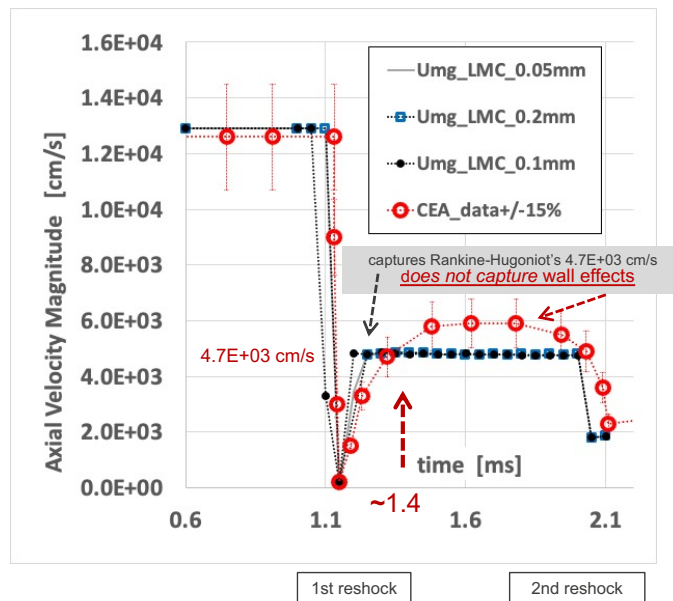


Figure 3: Axial velocity at $x=161\text{mm}$, ILES vs. CEA data.

Spectral content and standard deviation need to be prescribed for the initial material sharp-interface conditions. Following [16] IC are defined as superposition of six equally-weighted wavelengths in the neighborhood of h (characteristic initial *egg-crate* length and mix thickness), in addition to (red-noise) $\sim k^{-2}$ deformations with standard deviation $0.04h$ and shortest wavelength of at least 4 coarsest cells.

Mix width, as well as velocity magnitude and variance data from the experiments [19, 20] are used for benchmarking the ILES predictions – see [13] for more detailed discussion of validation results and analysis. In turn, ILES is then used as detailed reference for bridging results for same domain, resolution, and IC.

Compared to the actual CEA laboratory experiments [19], the computational domain in the present simulations (Fig.1) had the same (30cm) initial interface-to-wall distance. As runtime compromise – as in [16], we focused again on the center $5\text{cm} \times 5\text{cm}$ transverse portion of the laboratory channel window section with periodicity imposed in the transverse (y,z) directions – in contrast with $8\text{cm} \times 8\text{cm}$ channel cross-section limited by no-slip wall boundaries in the laboratory experiments. Thus, late-time discrepancies between computational and laboratory studies can be again expected due to effectively different boundary conditions in transverse directions, and unaccounted-for effects of near-wall momentum deficit in the actual experiments [20]. In [16], we found such disagreements after first reshock, for times $\gtrsim 1.4\text{ms}$.

Miscible gas-material interface modeling strategies have used various superpositions of perturbation modes [1] in the simulation of shock driven turbulence. The initial material interface thickness δ_o in the CEA laboratory experiments is not reported in the original paper [19] and was chosen in [20] to be a fraction the *egg crate* wavelength in the laboratory experiments ($h=1\text{mm}$). Our convenient computational resolution choice here is to use a single initial condition length-scale, with the same characteristic initial wavelength h used to prescribe $\delta_o=h$.

Compared to the actual CEA laboratory experiments [19], the computational domain in the present simulations (Fig.1) had the same (30cm) initial interface-to-wall distance. As runtime compromise – as in [16], we focused again on the center $5\text{cm} \times 5\text{cm}$ transverse portion of the laboratory channel window section with periodicity imposed in the transverse (y,z) directions – in contrast with $8\text{cm} \times 8\text{cm}$ channel

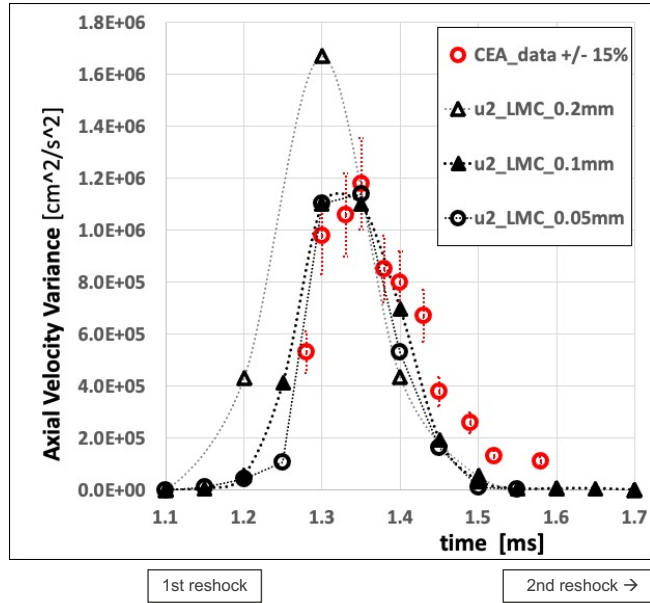


Figure 4: Axial velocity variance at x=161mm, ILES vs. CEA data.

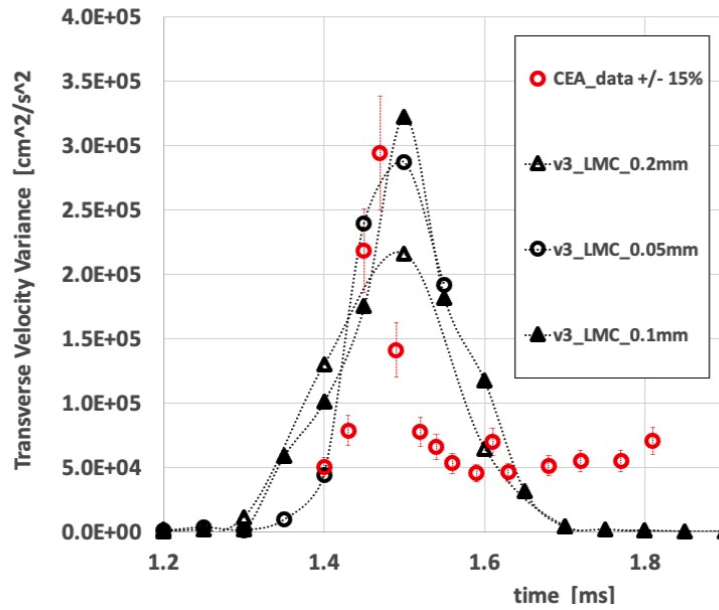


Figure 5: Transverse velocity variance at x=169mm, ILES vs. CEA data.

cross-section limited by no-slip wall boundaries in the laboratory experiments. Thus, late-time discrepancies between computational and laboratory studies can be again expected due to effectively different boundary conditions in transverse directions, and unaccounted-for effects of near-wall momentum deficit in the actual experiments [20]. In [16], we found such disagreements after first reshock, for times $\gtrsim 1.4$ ms.

2.1 xRAGE ILES Results

The present 3D simulations use between two and eight levels of AMR with finest resolutions ranging between 0.2mm and 0.05mm, respectively; the (more-practically motivated) 3D dynamic xRAGE-BHR bridging simulations below use 2 – 4 levels of AMR with 0.100mm 0.200mm resolution. The simulations typically used 0.1Billion (0.2mm resolution), 0.5B (0.1mm resolution), and up to 5.2B (0.05mm resolution) computational cells. We use the 3rd-order directionally-unsplitted LMC xRAGE numerical hydrodynamics [11, 12] as main strategy – vs. default directionally-split 2nd-order xRAGE used in [16].

Figures 2 illustrate SF6 mass fraction distributions near first-shock time – reflecting on IC characteristics, and at later times, before first reshock and after second reshock. Figures 3 and 4 compare the axial velocity magnitude and variance evolution vs. those in the reported CEA experiments [20]. As in the experiments, Fig. 3 shows a first velocity plateau near 130m/s corresponding to air accelerated by the incident shock wave, followed by a brief drop at 0m/s corresponding to air decelerated by the first reflected shock on the end wall, and then by a second perturbed plateau which includes the crossing of the turbulent mixture reflecting gradually on the density gradient in the turbulent mixing zone.

The present mean axial-velocity results for the latter plateau agree well with the experiments up to approximately $t \sim 1.3$ ms, and then agree with the theoretical mean velocity of 47m/s computed in [19] based on the Rankine-Hugoniot relations for transversely unbound flow (not affected by wall boundary layers). Reported differences between laboratory measured mean velocity (59m/s) and the said theoretical expectation (47m/s) have been attributed to the wall boundary-layer reversal effects in the SF6 at shock crossing.[20] As noted, the present simulations do not account for the wall boundary layer effects – and that consistently also underlies the discrepancies with experiments in Figs. 4 and 5 for $t \gtrsim 1.4$ ms. In agreement with the laboratory experiments, the second velocity plateau ends with the arrival of the second reflected shock wave on the end wall. The presently reported computed axial-velocity results are fairly independent of grid resolution.

Laboratory axial velocity variance (R11) data with $\pm 15\%$ estimated uncertainty was reported at locations of 161, 169 and 178.5 mm,[19] covering a range where turbulent mixing zone passages occur between its interactions with first and second reshock associated with the reflected shocks. Laboratory transverse velocity variance (R22) data was reported at the location 169 mm [20, 21]. At the location 161 mm – just after first reshock, Fig.4 shows a strong increase of the axial velocity variance was observed reaching a peak laboratory value of $117 (m/s)^2$, as the axial variance in the gaseous mixture has been excited by the first-reflected shock. Our results for R11 are consistent with those reported in the laboratory experiments – particularly so immediately after first reshock (finest 0.1mm and 0.05mm resolution LMC-xRAGE ILES results fall within reported $\pm 15\%$ uncertainty bar at the location 161 mm), and are fairly stable as function of grid resolution changes also for R22 (Fig.5). Highest values for R11 and R22 occur mostly just after the first reshock as in [19]. The peak R22 values quoted in [20] and [21] are fractions $\sim 1/3$ of their R11 counterparts – which is also consistent with our present findings.

2.2 Dynamic BHR Contribution Function and Mixing Simulation

As in [12], our 3D dynamic BHR simulations in this work use $q_{ij} = T_{ij}$ in conjunction with $l = 2$. We used between 2 – 8 levels of AMR with finest resolutions ranging between 0.2mm and 0.05mm, respectively. The (more-practically motivated) 3D dynamic xRAGE-BHR bridging simulations used 2 – 4 levels of AMR with finest 0.100mm resolution. The CEA shock-tube simulations used between 0.1-5.5 $\times 10^9$ computational cells.

Mixing measures less sensitive to subgrid contributions may enable accurate prediction of quantities of interest with the bridging-based generated LES with less resolution than typically required with the ILES high-fidelity option. Such potential benefits were noted in [12] with regard to having scalar-mixing predictions converged on coarser grids with the more-accurate LMC xRAGE. In what follows, we examine the impact of choices of the bridging length L in this context.

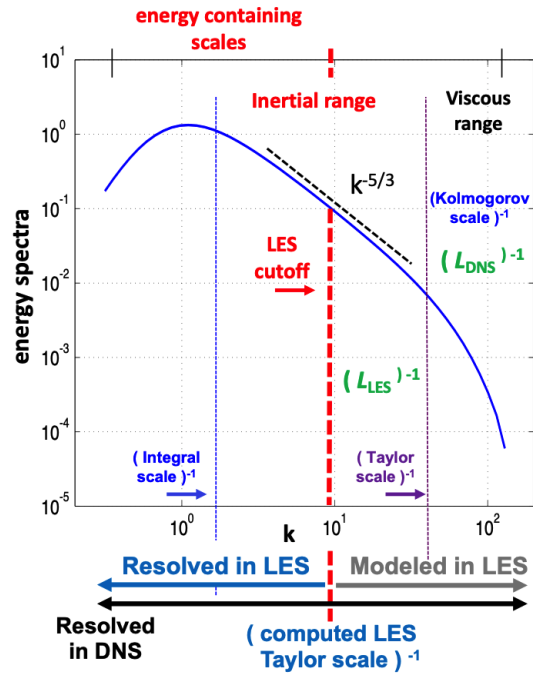


Figure 6: Bridging length L for RANS/DNS and RANS/LES hybrids.

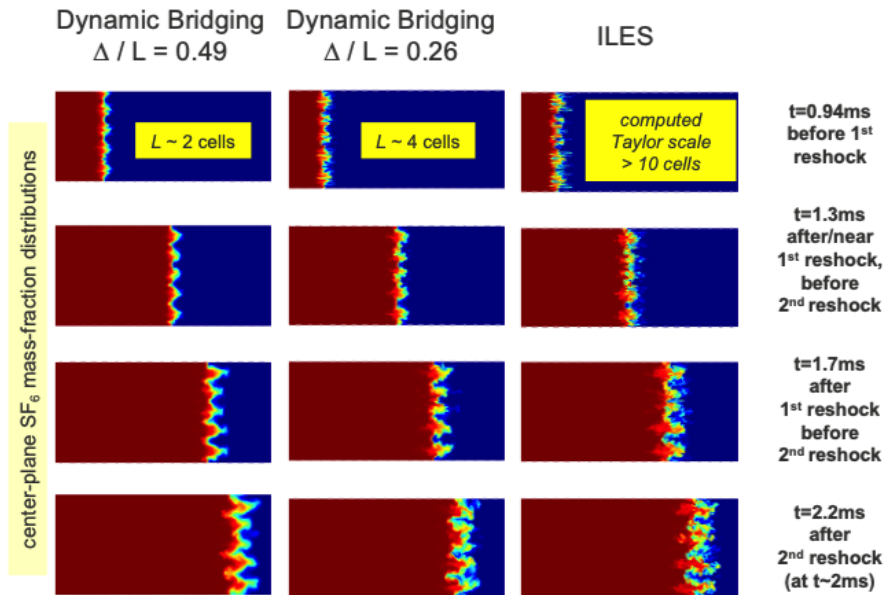


Figure 7: Dynamic BHR vs. ILES for 0.2mm resolution (two-level AMR).

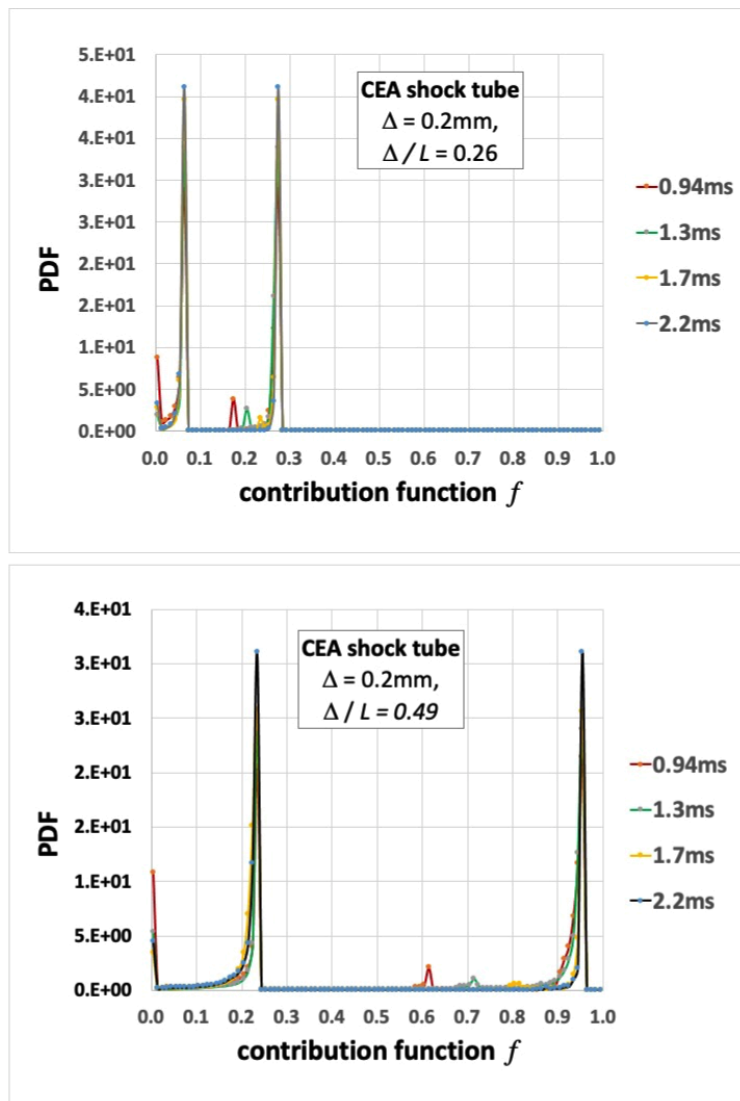


Figure 8: CEA shock-tube Dynamic BHR simulations; PDF of the contribution function vs. $\Delta x/L$ for the 0.2mm resolution case (two-level AMR)

Figure 7 shows centerplane predicted mass-fraction distributions associated with dynamic bridging and LMC-xRAGE ILES for the coarsest 0.2mm resolution (2-level AMR) case. Prediction accuracy is determined by ability to capture the vortical structures responsible for the onset and development of turbulence, and bridging modeling efficiency is directly determined by how much *less* resolution is required to resolve the flow scales not amenable to modeling [22]. Results with bridging length $L \sim 2$, and $L \sim 4$ (smallest) cells are shown at selected times before, after, and between the reshock events.

Varying the bridging length directly impacts the detailed captured content of space/time fluctuations effects with Dynamic BHR. Figure 8 shows probability distribution functions (PDF's) of the contribution function f over the whole 3D domain vs. $\Delta x/L$. Significantly smaller values ($f \sim 0.1 - 0.3$) indicate less contribution of RANS for $\Delta x/L = 0.26$, consistent with the corresponding results in Figure 7 – for which case increased captured content of space/time fluctuations effects are depicted. The suitability of this $\Delta x/L$ *sweet spot* value is confirmed in the Appendix in terms of the chevron shock-tube case [23, 24, 12].

For the sake of quantitative mix analysis, we consider here a frequently used integrated mixing measure – e.g. [23], $TMX = 4 \int \bar{\rho}^2 \bar{Y}_{air} \bar{Y}_{SF6} dx$, in terms of the mass density ρ , SF_6 and air mass fractions Y_{SF_6}

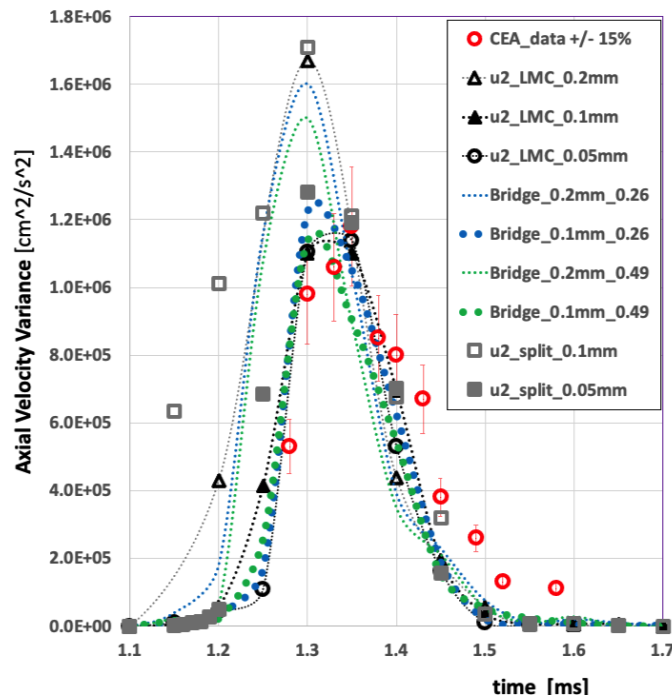


Figure 9: Axial velocity variance at $x=161\text{mm}$, ILES and Bridging *vs.* resolution, $\Delta/L = 0.26, 0.49$, and CEA data; ILES based on (present) LMC-unsplit and (previous [12]) split xRAGE are compared.

and $Y_{\text{air}} = 1 - Y_{\text{SF}_6}$, and using transverse-plane averaging, $\bar{\phi}(x) = \int \phi(x, y, z) dydz / \int dydz$.

The top portion of Figure 10 compares TMX *vs.* resolution and bridging length L . The ability of the dynamic bridging model to capture the basic mixing features with less resolution is well apparent between first and second reshock, where the 0.2mm and 0.1mm bridging predictions for $\Delta/L = 0.26$ are nearly the same and in very good agreement with the finest (0.05mm) ILES – suggesting preferred bridging/resolution trade-offs and robust mixing capturing with coarser gridding. On the other hand, we note the axial velocity variance results in Fig.9 – between first and second reshock – exemplify similar velocity turbulence features captured with dynamic bridging and ILES as function of grid resolution, indicating that the dynamic bridging modeling does not appear to provide much added improvement on the turbulent velocity fluctuations predictions for a given resolution. This suggests that an explicit subgrid scale component in (1) may be needed for the coarsest grid resolutions – see [13] for the extended dynamic bridging formalism.

Beyond second reshock, bridging with 0.1mm resolution and $\Delta/L = 0.26$ still provides good predictions – albeit RANS corrections to better converged (resolved) ILES appear unnecessary there. This is confirmed in the bottom part of Figure 10, where the focus is on the case $\Delta/L = 0.26$, and on examining Dynamic BHR simulations restarted at time 1.6ms (before 2nd reshock) and continued thereafter with RANS contributions turned off (i.e., pure ILES); significantly improved mixing predictions are thus achieved after 2nd reshock for both resolutions. The latter results suggest that imposing additional late-time constraints on f might be helpful, e.g., by requiring that f vanish at late times when conditions are met in terms of a suitable progress variable characterizing transition and small-scale population (e.g., as function of λ_c).

3 Summary and Conclusions

We revisited coarse-grained simulation strategies for turbulent material mixing applications involving shock-driven turbulence in the context of LANL’s Eulerian xRAGE hydrodynamics and BHR RANS codes, using the newly-available more-accurate LMC xRAGE hydrodynamics. xRAGE ILES and a recently proposed [12] dynamic ILES/RANS bridging strategy for applications involving variable-density turbulent mixing applications were tested. The bridging approach is based on the FSM [6, 7], locally blending a high fidelity

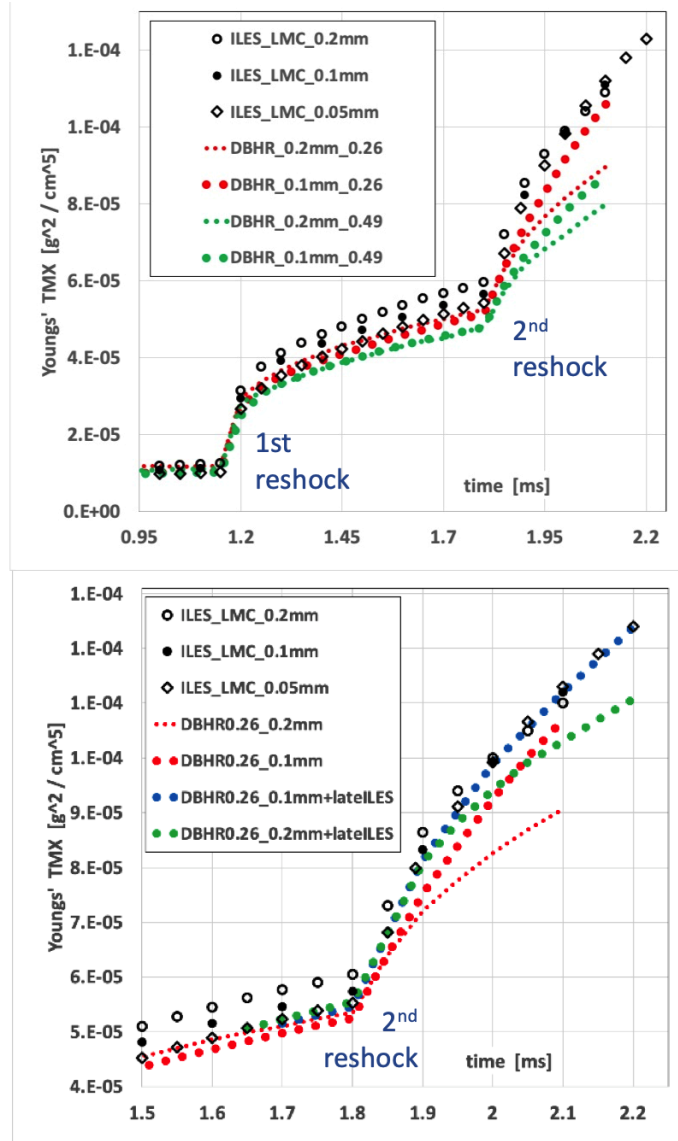


Figure 10: TMX for LMC-xRAGE ILES and Dynamic BHR vs. resolution for $\Delta/L = 0.26, 0.49$ (top); for $\Delta/L = 0.26$, results for Dynamic BHR + late-time ILES are also included (pure ILES after time 1.6ms) – focusing on improved mixing prediction after 2nd reshock (bottom).

computational strategy with RANS modeling – depending on how much of the turbulence is resolved at given resolution, and providing a realizable LES strategy in-between. How much dissipation is modeled and how much is computed is decided based on having the RANS model locally morph into an LES SGS model, through the contribution function.

Our bridging strategy follows a proposal by Germano [9] to solve for f dynamically, based on decomposing the full stress into modeled and resolved components, using a differential filter as secondary filtering operation [10] to define the resolved stress, and additionally requiring the resolved stress to approach the full stress with grid resolution refinement [12] to ensure realizability of the bridging-based LES. This is in contrast with the classical FSM defining the contribution functions explicitly in terms of local Δ in empirical *ad hoc* fashion [6, 7]. We expect the present dynamic hybrid strategy to be also applicable for converging geometries and to be applicable as well with other LES and RANS approaches.

Case studies of interest involved relevant shock tube experiments prototyping shock-driven turbulent

mixing for which evolution of mix-width, velocity magnitude and variances are available for benchmarking. Much improved scale-resolving with LMC-xRAGE ILES and with dynamic LMC-xRAGE / BHR bridging enables higher simulated mixing and turbulence levels on coarser grids. For the tested planar shock tube case, the more-accurate models can achieve the same level of accuracy with less resolution than required with the highest-fidelity turbulence simulation models typically used at scale with default xRAGE hydrodynamics [13]. Two levels of grid-coarsening savings can be achieved for mixing predictions in these comparisons: one associated with the more-accurate LMC xRAGE hydrodynamics, and an additional one from using the dynamic xRAGE-BHR bridging. Savings of $2\times$ to $4\times$ on grid size are possible – i.e., $8\times$ to $64\times$ fewer points over the 3D domain.

4 Appendix: Additional Contribution function analysis.

We revisit here the chevron shock-tube simulations [23, 24, 12] involving high (SF_6) and low (air) density gases initially separated by membranes and wire mesh as indicated schematically in Figure 11. ILES computations simulating these experiments have been previously reported [23, 24]. The growth of the Richtmyer-Meshkov (RM) instability and characteristic turbulent mixing measures were studied using interface perturbations involving prescribed spectral content and standard deviation *s.d.*. The SF_6 and air are assumed to be initially in temperature and pressure equilibrium at 1 bar, with densities of 6.34 kg/m^3 and 1.184 kg/m^3 , respectively, yielding $\gamma = 1.4$ and $\gamma = 1.076$. A shocked air region is created upstream in terms of a higher-density higher-pressure region chosen to satisfy the Rankine-Hugoniot relations for a $Ma = 1.26$ shock. The simulations are carried out in a reference frame in which the air- SF_6 interfaces are initially at rest. The shock propagates in the (x) direction through the contact discontinuity and reflects at the right (reflective) boundary. Uniform cartesian gridding with smallest grid sizes Δ of 1/16 cm and 1/32 cm were employed in our earlier simulations [24, 12] – having $\Delta/L = 0.21, 0.10$, respectively [11].

AMR with grid sizes ranging between (1/4 cm - 1/16 cm) and (1/4 cm - 1/32 cm) and fixed $\Delta/L = 0.25$ were considered. Figure 12 illustrates the centerplane full-domain AMR fine-resolution gridding at late-time ($t=3.09\text{ms}$), and the dotted-contours indicate the selected sub-domain in the visualizations. Representative temporal evolution of centerplane visualizations of SF_6 mass-fraction and f distributions are shown in Figures 13. Corresponding full-domain PDF's of f for the selected times and both grid resolutions presented in Figure 14, indicate relatively-small RANS contributions ($f < 0.3$) for $\Delta/L = 0.25$ – consistent with $\Delta/L = 0.26$ being a convenient working choice for Dynamic BHR in the CEA shock-tube case above. Finally, sensitivities to grid resolution shown in Figure 15 clearly depict robustness of the late time mixing predictions.

5 Acknowledgements

The author thanks David Youngs for helpful discussions. Los Alamos National Laboratory is operated by TRIAD LLC for US DOE NNSA. This research was supported by the LANL PEM Mix & Burn Project.

References

- [1] Grinstein, F.F., Coarse Grained Simulation and Turbulent Mixing, Cambridge, NY, 2016.
- [2] Zhou, Y., Grinstein, F.F., Wachtor, A.J., and Haines, B.M., Estimating the effective Reynolds number in implicit large-eddy simulation, Phys. Rev. E, 89, 013303, 2014.
- [3] Grinstein, F.F., Margolin, L.G., Rider, W.J., Implicit Large Eddy Simulation: Computing Turbulent Flow Dynamics, Cambridge, NY, 2nd printing, 2010.
- [4] Ghosal, S., An analysis of numerical errors in large-eddy simulations of turbulence, J. Comput. Phys., 125, 187-206, 1996.
- [5] Frolich J and von Terzi, D.A., Hybrid LES/RANS methods for the simulation of turbulent Flows, Progress in Aerospace Sciences, 44, 349-77, 2008.
- [6] Speziale, C. G., A Combined Large-Eddy Simulation and Time-Dependent RANS Capability for High-Speed Compressible Flows, AIAA Journal, 36(2), 173-184, 1998.

- [7] Fasel, H.F., von Terzi, D.A., and Sandberg, R.D., A Methodology for Simulating Compressible Turbulent Flows, *J. Appl. Mech.*, 73, 405-412, 2006.
- [8] Germano, M., Turbulence: The Filtering Approach, *J. Fluid Mechanics*, 238, 325-336, 1992.
- [9] Germano, M., Comment on Turbulence Modeling for Time-Dependent RANS and VLES: A Review, *AIAA Journal*, 36(9), 1766-1767, 1998.
- [10] M. Germano. Differential filters for the large eddy numerical simulation of turbulent flows. *The Physics of Fluids*, 29(6):1755-1757, 1986.
- [11] F.F. Grinstein, F J.A. Saenz, J.C. Dolence, T.O. Masser, R.M. Rauenzahn, M.M. Francois, Effects of operator splitting and low Mach-number correction in turbulent mixing transition simulations, *Computers and Mathematics with Applications*, 78, 437-458, 2019.
- [12] F.F. Grinstein, J.A. Saenz, R.M. Rauenzahn, M. Germano, and D.M. Israel, Dynamic Bridging Modeling for Coarse Grained Simulations of Shock Driven Turbulent Mixing *Computers and Fluids*, 199, 104430, 2020.
- [13] Grinstein, F.F., Saenz, J.A., and Germano, M., Coarse Grained Simulations of Shock-Driven Turbulent Material Mixing, *Phys. Fluids*, 33, 035131, 2021.
- [14] F.F. Grinstein, F. S. Pereira, W.J. Rider, Numerical Approximations Formulated as LES Models, invited chapter in *Numerical Methods in Turbulence Simulation*, edited by Robert D. Moser, Springer, 2022.
- [15] Gittings, M., Weaver, R., Clover, M., Betlach, T., Byrne, N., Coker, R., Dendy, E., Hueckstaedt, R., New, K., Oakes, W.R., Ranta, D., Stefan, R., The RAGE radiation hydrodynamic code, *Comput. Science & Discover* 1, 015005, 2008.
- [16] F.F. Grinstein, Initial Conditions and Modeling for Simulations of Shock Driven Turbulent Material Mixing, *Computers and Fluids*, 151, pp. 58-72, 2017.
- [17] Wachtor, A.J., Grinstein F.F., Devore, C.R., Ristorcelli, J.R., and Margolin, L.G., Implicit Large-Eddy Simulations of Passive Scalar Mixing in Statistically Stationary Isotropic Turbulence, *Physics of Fluids*, 25, 025101 (2013).
- [18] F.F. Grinstein, Coarse Grained Simulation of Convectively Driven Turbulent Mixing Transition and Turbulence Decay, *Physica D: Nonlinear Phenomena*, 407, 132419, 2020.
- [19] Poggi, F., Thorembey, M-H. and Rodriguez, G., Velocity measurements in turbulent gaseous mixtures induced by Richtmyer-Meshkov instability, *Phys. Fluids*, 10, 2698, 1998.
- [20] C. Mugler and S. Gauthier, Two-dimensional Navier-Stokes simulations of gaseous mixtures induced by Richtmyer-Meshkov instability, *Phys. Fluids* 12 (2000), p. 1783.
- [21] Grégoire, O., Souffland, D. and Gauthier, S., A second-order turbulence model for gaseous mixtures induced by Richtmyer-Meshkov instability, *Journal of Turbulence*, 6, 1, 2005.
- [22] F. S. Pereira, L. Eça, G. Vaz, S. S. Girimaji, Challenges in Scale-Resolving Simulations of turbulent wake flows with coherent structures, *Journal of Computational Physics*, 363, pp.98-115, 2018.
- [23] Hahn, M., D. Drikakis, D. L. Youngs, & R. J. R. Williams, Richtmyer-Meshkov turbulent mixing arising from an inclined material interface with realistic surface perturbations and reshocked flow, *Phys. Fluids*, 23, 046101, 2011.
- [24] Haines, B.M., F.F. Grinstein, and J.D. Schwarzkopf, Reynolds-averaged Navier-Stokes initialization and benchmarking in shock-driven turbulent mixing, *Journal of Turbulence*, 14:2, 46-70, 2013.
- [25] Besnard, D., Harlow, F.H., Rauenzahn, R.M., and Zemach, C., Turbulence transport equations for variable-density turbulence and their relationship to two-field models, LA-UR- 12303, Los Alamos National Laboratory, 1992.
- [26] Schwarzkopf, J.D., Livescu, D., Gore, R.A., Rauenzahn, R.M., Ristorcelli, J.R., Application of a second-moment closure model to mixing processes involving multi-component miscible fluids, *Journal of Turbulence*, 12, No. 49, pp. 1-35, 2011.
- [27] J. D. Schwarzkopf, D. Livescu, J. R. Baltzer, R. A. Gore, J. R. Ristorcelli, A two-length scale turbulence model for single-phase multi-fluid mixing, *Flow Turbulence Combust*, 96:1-43, 2016.

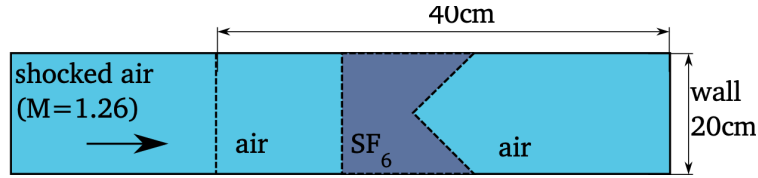


Figure 11: Schematic of the chevron shock tube.

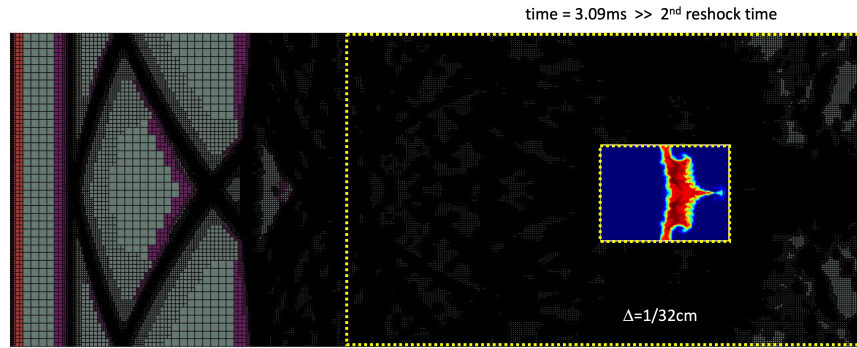


Figure 12: Chevron shock-tube Dynamic BHR simulations; late-time ($t=3.09\text{ms}$) full-domain AMR fine-resolution ($1/4\text{cm}-1/32\text{cm}$ grid for $\Delta/L = 0.25$; dotted-contours indicate the selected sub-domain in the visualizations).

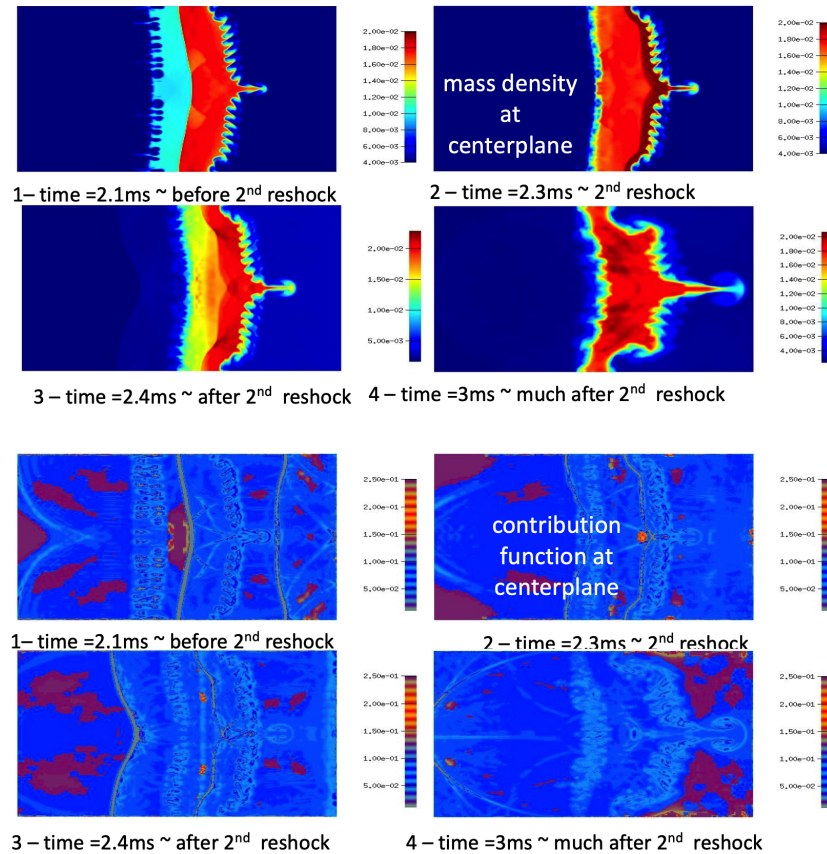


Figure 13: Chevron shock-tube Dynamic BHR simulation results for $\Delta/L = 0.25$.

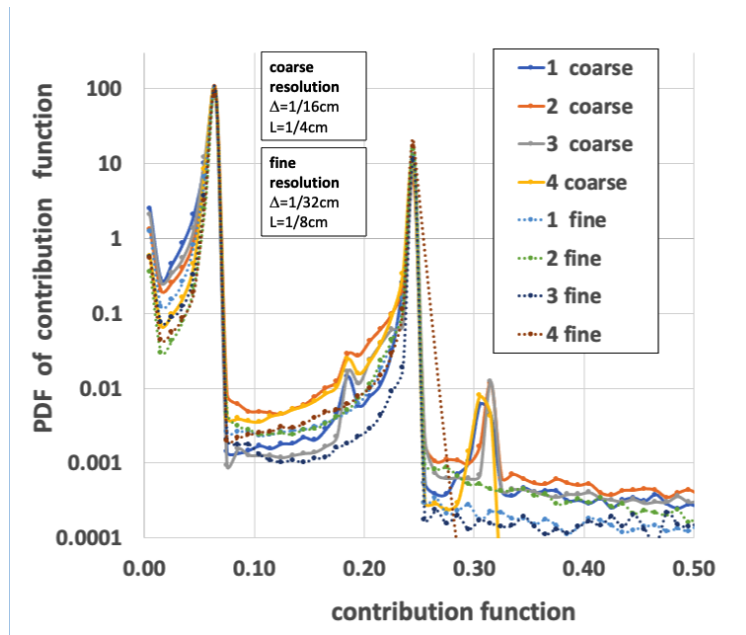


Figure 14: Chevron shock-tube Dynamic BHR simulations; PDF of the contribution function for $\Delta/L = 0.25$.

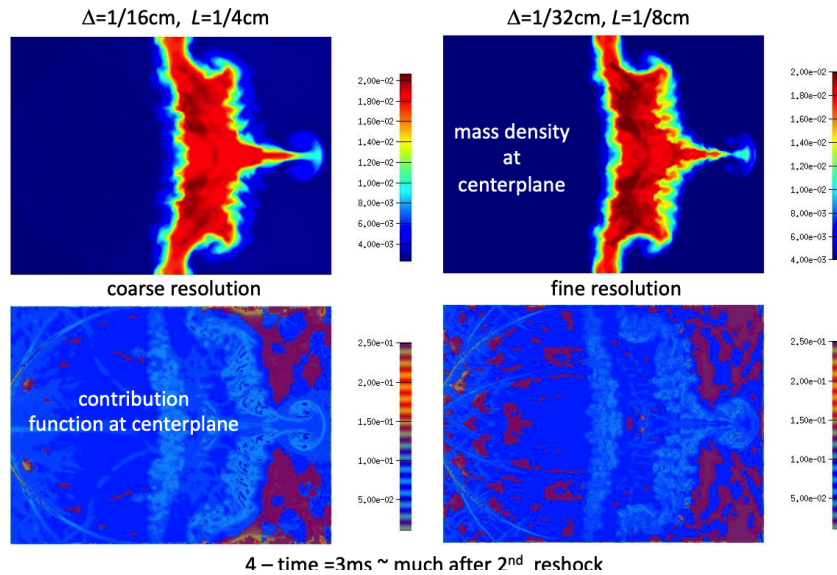


Figure 15: Chevron shock-tube Dynamic BHR simulations, late-time ($t=3.09\text{ms}$) sample results vs. grid resolution for $\Delta/L = 0.25$.